

Article

# Integrated Control of Spray System and Active Suspension Systems Based on Model-Assisted Active Disturbance Rejection Control Algorithm

Jianxu Zhu <sup>1</sup>, Dingxuan Zhao <sup>1,\*</sup>, Shuang Liu <sup>2</sup>, Zilong Zhang <sup>1</sup>, Guangyu Liu <sup>1</sup> and Jinming Chang <sup>1</sup><sup>1</sup> School of Mechanical Engineering, Yanshan University, Qinhuangdao 066004, China<sup>2</sup> School of Electrical Engineering, Yanshan University, Qinhuangdao 066004, China

\* Correspondence: zdx@ysu.edu.cn; Tel.: +86-33-5807-8106

**Abstract:** Due to the lack of body stability of emergency rescue vehicles, their attitude stability is insufficient and they are unable to realize working while driving, resulting in low rescue efficiency. Aiming at the water tower fire truck, which is equipped with an active suspension system, the vehicle attitude stability is studied. First, combined with the active suspension system and spray system, a 13-DOF integrated dynamic model for the water tower fire truck is established. Using the model-assisted active disturbance rejection control method, the controllers are designed for the vertical displacement, pitch angle, and roll angle of the vehicle attitude. Then, the computer simulation is carried out to verify the effectiveness of this control method. Finally, the water spray obstacle crossing experiment is carried out with a JP32G water tower fire truck. The results show that when the vehicle runs over the triangular obstacle on one side and two sides in the integrated spray-active suspension mode, the peak–peak values of body pitch angle and roll angle are reduced by 10.9% and 23.2%, and 23.7% and 16.3%, respectively, compared with the passive hydro pneumatic suspension.



**Citation:** Zhu, J.; Zhao, D.; Liu, S.; Zhang, Z.; Liu, G.; Chang, J. Integrated Control of Spray System and Active Suspension Systems Based on Model-Assisted Active Disturbance Rejection Control Algorithm. *Mathematics* **2022**, *10*, 3391. <https://doi.org/10.3390/math10183391>

Academic Editor: Junseok Kim

Received: 3 August 2022

Accepted: 14 September 2022

Published: 19 September 2022

**Publisher's Note:** MDPI stays neutral with regard to jurisdictional claims in published maps and institutional affiliations.



**Copyright:** © 2022 by the authors. Licensee MDPI, Basel, Switzerland. This article is an open access article distributed under the terms and conditions of the Creative Commons Attribution (CC BY) license (<https://creativecommons.org/licenses/by/4.0/>).

**Keywords:** water tower fire truck; active suspension; MADRC; vehicle attitude stability**MSC:** 93D15

## 1. Introduction

With the acceleration of urbanization and the improvement of people's living standards, disaster prevention and mitigation, public safety, and emergency hedging have attracted increasingly more attention. Emergency rescue is characterized by uncertainty, unexpectedness, and complexity. The chassis of existing emergency rescue vehicles is restricted by their poor mobility and insufficient vehicle attitude stability, which leads to low rescue efficiency. For example, when a water tower fire truck is working, the traditional suspension system cannot satisfy the requirement of vehicle posture stability. When working, the whole vehicle needs to be supported at a fixed place by outriggers, which makes it impossible for the vehicle to work while driving. The scope of work is limited and the rescue efficiency is not high. If the water tower fire truck is operated while driving, its operation efficiency can be improved, and the rescue time can be saved, which is of great significance to ensure the safety of personnel and property.

The water tower fire truck is equipped with a high-power fire pump and a fire monitor. The fire monitor will produce a jet reaction force, resulting in a large roll and pitch moment acting on the body. At the same time, the boom of the water tower fire truck will be deployed, resulting in the increase in the center of gravity of the whole vehicle. These factors seriously affect the pose stability of the vehicle. In addition, when the vehicle is driving, the road surface is uneven and sometimes full of explosives such as gravel. When working on uneven terrain, the vehicle may roll over [1]. Therefore, to realize the operation while driving, the water tower fire truck requires the body to have better posture stability,

which puts forward higher requirements for the regulation performance of the vehicle suspension system. The suspension system is an important part of the vehicle chassis, and its performance directly determines the ride comfort, operating stability, and driving safety of the vehicle [2–4].

The active suspension system can adjust the output of the actuator in real-time according to the changes in road input and vehicle state [5–7]. Obtaining a better shock absorption and body posture control effect provides the possibility to realize the operation while driving the water tower fire truck.

At present, much research effort has been devoted to the control synthesis of active suspension systems, such as model predictive control [8], preview control [9], adaptive control [10,11], fault-tolerant control [12], and event-triggered control [13]. The above control methods have improved the performance of vehicles to varying degrees, and many scholars have studied vehicle attitude stability. Kim and Lee [14] proposed a new nonlinear controller to adjust the height of the vehicle sprung mass and to regulate the roll and pitch angles of the vehicle body by an air suspension system. Youn et al. [15] designed an attitude tracking controller with zero acceleration as the target and simulated the feasibility of the attitude tracking controller by using a 4-DOF half-car model. Westhuizen et al. [16] proposed the possibility of using slow active suspension control to reduce the body roll and, thus, reduce the rollover tendency. Tchamna [17] studied a variable-stiffness semi-active suspension system to control vehicle attitude under cornering conditions. Chen [18] proposed an attitude control strategy for heavy emergency rescue vehicles based on the road level. For different road grades, the control parameters of the active suspension system are changed to reduce the root-mean-square values of the vertical acceleration, pitch angle, and roll angle of the vehicle body. Youn [19] studied the attitude control method of the vehicle body and calculated the ideal driving posture of the vehicle to offset the lateral and longitudinal forces acting on the passengers. The simulation results showed that this method has great potential. He [1] analyzed the impact of fire monitors under different working conditions on the static rollover angle of fire engines. The results showed that when the fire monitor works under high pressure, the influence on the static rollover angle of the vehicle can reach  $15.8^\circ$ . By establishing a virtual prototype model, Sun et al. [20] analyzed the influence of jet reaction force on the lateral stability of urban main fire trucks. The results showed that when the water flow velocity of the fire monitor is 30 L/s to 120 L/s, the rollover angle of the fire engine ranges from  $30.9^\circ$  to  $20.57^\circ$ . Gong et al. [21] proposed a semi-active suspension variable damping control strategy for heavy vehicles using a 9-DOF vehicle mode with improved vehicle ride comfort and handling stability. Wang et al. [22] presented a vehicle attitude compensation algorithm based on the state observer for a vehicle semi-active suspension system, improved the ride comfort of magneto-rheological suspension, and optimized the vehicle body attitude under braking and steering states. Li et al. [23] developed a centralized-distributed control strategy with attitude information obtained by multi-sensor fusion. The proposed attitude control system improved the obstacle performance, mobility, and flexibility of the vehicles. Guo [24] made the multi-axle emergency rescue vehicle equivalent to a 3-degrees-of-freedom parallel mechanism; the action of the servo actuator was driven by solving the inverse solution of the parallel mechanism position. Zeng et al. [25] presented an aperiodic adaptive intermittent control scheme to stabilize the attitude of the vehicle by using the backstepping technique.

The above research on vehicle attitude mainly focused on body attitude control under steering or stationary conditions. Few papers have been published on the body stability of the water tower fire truck while driving. Most of the models used in the current literature have been quarter-car or half-car suspension models, and only the vertical attitude or the pitch angle has been considered, which is not practical in industrial applications. Although the whole vehicle suspension system model has been used in the literature [14,15,18,22–24], the dynamic model of the working device mounted on the vehicle has not been considered. These models are not accurate enough for the water tower fire truck. Although the literature [1,20] has studied the effects of the reaction force on the vehicle, they have not



## 2. Dynamic Model of Spray-Active Suspensions Integrated System

### 2.1. Reaction Force Calculation of Fire Monitor

The high pressure and high flow working environment of the fire monitor will certainly result in a large reaction force, which will affect the operation stability of the fire truck. Therefore, it is necessary to calculate the reaction force. The direction of the reaction force acting on the fire monitor is opposite to that of the water flow. According to the Navier–Stokes equation of the fluid, the ANSI Standard Specification gives the following general expressions for calculating the jet reaction force.

$$F = - \int_{C.V.} \frac{d}{dt}(\rho u) dV + \int_{C.S.} \rho u(u \cdot dA) + \int_{A_{in}} p dA_{in} + \int_{A_{out}} p dA_{out} - \int_{A_{pipe}} p_a dA_{pipe} \quad (1)$$

where  $F$  represents the reaction force,  $\rho$  represents density of the fluids,  $u$  represents the velocity of the fluid,  $p$  represents the pressure at the center of unit area,  $p_a$  represents the pressure of the environment around the pipe,  $V$  represents the volume of the control volume,  $A$  represents the area of the control volume,  $A_{in}$  represents the area that flows into the control volume,  $A_{out}$  represents the area that flows out of the control volume,  $A_{pipe}$  represents the external area of the pipe,  $C.V.$  represents the control volume, and  $C.S.$  represents the control surface.

In the formula, there is no assumption or simplified calculation, and it is based on the most basic principles of the fluid force, so it is accurate and universal. There are many integral operations in the general formula, which are difficult to apply in the actual project. It needs to be further simplified.

Assume that the flow of water in the fire monitor is one-dimensional.

When the fluid reaches a steady state, the above equation can be simplified as [28]

$$F_l = \rho_e u_e^2 A_e - A_e(p_e - p_a) \quad (2)$$

where  $\rho_e$  represents the density of the fluids,  $F_l$  represents the steady-state jet reaction force,  $u_e$  represents the fluid velocity,  $p_e$  represents fluid pressure,  $A_e$  represents the area of the fire monitor outlet, and  $p_a$  represents the surrounding pressure around the fire monitor.

### 2.2. Integrated Dynamic Model

The 13-DOF integrated dynamic model of the active suspension and the spray system is shown in Figure 1.

The 13 degrees of freedom in this model are 6 unsprung mass vertical movements; the vertical, roll, and pitch movements of the vehicle; the luffing, rotation of the boom, and the swing motion of the fire monitor in two directions. There are six suspension actuating units in the model;  $z_{bi}$  represents vertical displacement at the hinge point of the suspension and chassis ( $i = 1, 2, 3, 4, 5, 6$ ),  $m_{wi}$  represents each unsprung mass,  $z_{wi}$  represents the vertical displacement of each unsprung mass,  $c_{si}$  represents the damping coefficient,  $k_{si}$  represents the stiffness of the suspension,  $l$  represents the wheel tread, and  $k_{ti}$  represents the stiffness of the tire.

Assume that the mass of the boom is concentrated at the center of mass; according to Newton’s second law, the following equations of motion for the heave, pitch, and rolling of a vehicle can be obtained.

$$m_b \ddot{Z} = k_{s1}(z_{w1} - z_{b1}) + c_{s1}(\dot{z}_{w1} - \dot{z}_{b1}) + U_1 + k_{s2}(z_{w2} - z_{b2}) + c_{s2}(\dot{z}_{w2} - \dot{z}_{b2}) + U_2 + k_{s3}(z_{w3} - z_{b3}) + c_{s2}(\dot{z}_{w3} - \dot{z}_{b3}) + U_3 + k_{s4}(z_{w4} - z_{b4}) + c_{s2}(\dot{z}_{w4} - \dot{z}_{b4}) + U_4 + k_{s5}(z_{w5} - z_{b5}) + c_{s2}(\dot{z}_{w5} - \dot{z}_{b5}) + U_5 + k_{s6}(z_{w6} - z_{b6}) + c_{s2}(\dot{z}_{w6} - \dot{z}_{b6}) + U_6 - F_l \sin \alpha \quad (3)$$

$$\begin{aligned} \ddot{\theta} I_{\theta} = & -a[k_{s1}(z_{w1} - z_{b1}) + c_{s1}(\dot{z}_{w1} - \dot{z}_{b1}) + U_1 + k_{s2}(z_{w2} - z_{b2}) + c_{s2}(\dot{z}_{w2} - \dot{z}_{b2}) + U_2] \\ & + b[k_{s3}(z_{w3} - z_{b3}) + c_{s2}(\dot{z}_{w3} - \dot{z}_{b3}) + U_3 + k_{s4}(z_{w4} - z_{b4}) + c_{s2}(\dot{z}_{w4} - \dot{z}_{b4}) + U_4] \\ & + c[k_{s5}(z_{w5} - z_{b5}) + c_{s2}(\dot{z}_{w5} - \dot{z}_{b5}) + U_5 + k_{s6}(z_{w6} - z_{b6}) + c_{s2}(\dot{z}_{w6} - \dot{z}_{b6}) + U_6] \\ & + F_l [\cos \alpha \sin(\beta + \gamma) \sin \delta B + \sin \alpha (d - B \cos \delta \cos \gamma)] \end{aligned} \quad (4)$$

$$\begin{aligned} \ddot{\varphi} I_{\varphi} = & \frac{1}{2} [k_{s1}(z_{w1} - z_{b1}) + c_{s1}(\dot{z}_{w1} - \dot{z}_{b1}) + U_1 + k_{s3}(z_{w3} - z_{b3}) + c_{s2}(\dot{z}_{w3} - \dot{z}_{b3}) + U_3 \\ & + k_{s5}(z_{w5} - z_{b5}) + c_{s2}(\dot{z}_{w5} - \dot{z}_{b5}) + U_5] - \frac{1}{2} [k_{s2}(z_{w2} - z_{b2}) + c_{s2}(\dot{z}_{w2} - \dot{z}_{b2}) + U_2 \\ & + k_{s4}(z_{w4} - z_{b4}) + c_{s2}(\dot{z}_{w4} - \dot{z}_{b4}) + U_4 + k_{s6}(z_{w6} - z_{b6}) + c_{s2}(\dot{z}_{w6} - \dot{z}_{b6}) + U_6] \\ & - F_l [\cos \alpha \cos(\beta + \gamma) B \sin \delta - s B \sin \alpha \sin \delta \sin \gamma] \end{aligned} \tag{5}$$

where  $Z$ ,  $\theta$ , and  $\varphi$  represent vertical displacement, pitch angle, and roll angle of the vehicle, respectively;  $m_b$  represents a sprung mass;  $m_b = m_{a1} + m_{a2}$ ;  $m_{a1}$  represents the chassis part of the sprung mass;  $m_{a2}$  represents the boom part of the sprung mass;  $\alpha$  represents the angle between the jet reaction force and horizontal direction;  $\beta$  represents the angle between the jet reaction force and vertical direction;  $a$  represents the distance between the front axle and mass center of the chassis;  $b$  represents the distance between the middle axle and mass center of the chassis;  $c$  represents the distance between the rear axle and the mass center of the chassis;  $d$  represents the distance between the hinge of the boom and chassis and the mass center of the chassis;  $\delta$  represents the luffing angle of the boom;  $\gamma$  represents the rotating angle of the boom;  $B$  represents the length of the boom;  $B_1$  represents distance from the hinge point of the boom and chassis to the mass center of the boom;  $I_{\theta 1}$  represents the pitching moment of inertia of the chassis part;  $I_{\varphi 1}$  represents the rolling moment of inertia of the chassis part;  $I_{\theta}$  represents the equivalent pitching moment of inertia of the vehicle;  $I_{\varphi}$  represents the equivalent rolling moment of inertia of the vehicle body.

The calculation method of the equivalent pitch and roll moment of inertia of the vehicle body is as follows:

$$I_{\theta} = I_{\theta 1} + m_a \sqrt{(B_1 \sin \delta)^2 + (d - B_1 \cos \delta \cos \gamma)^2} \tag{6}$$

$$I_{\varphi} = I_{\varphi 1} + m_a \sqrt{(B_1 \sin \delta)^2 + (B_1 \cos \delta \sin \gamma)^2} \tag{7}$$

The vertical dynamic equation of the six wheels is

$$m_{wi} \ddot{z}_{wi} = k_{si}(z_{bi} - z_{wi}) - k_{ti}(z_{wi} - z_{ri}) + c_{si}(\dot{z}_{bi} - \dot{z}_{wi}) - U_i \tag{8}$$

where  $z_{ri}$  represents the road input of the  $i$ th wheel.

As the pitch and roll angles of the vehicle are small, it can be considered that  $\sin \theta \approx \theta$ ,  $\sin \varphi \approx \varphi$ . Suppose that the vehicle is a rigid body; according to the motion law of a rigid body, the vertical displacement of the hinge joint between the suspension and chassis can be obtained:

$$z_{b1} = Z_b - a \sin \theta - l/2 \sin \varphi \approx Z_b - a\theta - l/2\varphi \tag{9}$$

$$z_{b2} = Z_b - a \sin \theta + l/2 \sin \varphi \approx Z_b - a\theta + l/2\varphi \tag{10}$$

$$z_{b3} = Z_b + a \sin \theta - l/2 \sin \varphi \approx Z_b + a\theta - l/2\varphi \tag{11}$$

$$z_{b4} = Z_b + a \sin \theta + l/2 \sin \varphi \approx Z_b + a\theta + l/2\varphi \tag{12}$$

$$z_{b5} = Z_b + a \sin \theta - l/2 \sin \varphi \approx Z_b + a\theta - l/2\varphi \tag{13}$$

$$z_{b6} = Z_b + a \sin \theta + l/2 \sin \varphi \approx Z_b + a\theta + l/2\varphi \tag{14}$$

Select the vehicle system state vector  $X$  as follows:

$$X = [Z \ \theta \ \varphi \ z_{b1} \ z_{b2} \ z_{b3} \ z_{b4} \ z_{b5} \ z_{b6} \ z_{w1} \ z_{w2} \ z_{w3} \ z_{w4} \ z_{w5} \ z_{w6} \ \dot{Z} \ \dot{\theta} \ \dot{\varphi} \ \dot{z}_{w1} \ \dot{z}_{w2} \ \dot{z}_{w3} \ \dot{z}_{w4} \ \dot{z}_{w5} \ \dot{z}_{w6}] \tag{15}$$

Then, the system equation is expressed as

$$\dot{X} = AX + BU + W \tag{16}$$

where  $A$  is the coefficient matrix of vector  $X$ ,  $B$  is the coefficient matrix of vector  $U$ ,  $W$  represents external disturbance, and  $U$  is the road profile of each wheel and the active output force of each actuator.

$$\mathbf{U} = [z_{r1} \ z_{r2} \ z_{r3} \ z_{r4} \ z_{r5} \ z_{r6} \ U_1 \ U_2 \ U_3 \ U_4 \ U_5 \ U_6] \tag{17}$$

$$\mathbf{W} = [w_1 \ w_2 \ w_3] \tag{18}$$

$$w_1 = -F_l \sin \alpha \tag{19}$$

$$w_2 = F_l [\cos \alpha \sin \beta \sin \delta B + \sin \alpha] \tag{20}$$

$$w_3 = -F_l \cos \alpha \cos \beta \sin \delta B \tag{21}$$

Select the vertical displacement, pitch angle, roll angle, and the corresponding speed, acceleration of the vehicle body, the suspension, and the tire displacement to form the output vector  $Y$ :

$$Y = [Z \ \theta \ \varphi \ \dot{Z} \ \dot{\theta} \ \dot{\varphi} \ \ddot{Z} \ \ddot{\theta} \ \ddot{\varphi} \ z_{b1} \ z_{b2} \ z_{b3} \ z_{b4} \ z_{b5} \ z_{b6} \ z_{w1} \ z_{w2} \ z_{w3} \ z_{w4} \ z_{w5} \ z_{w6}] \tag{22}$$

The output equation of the system can be expressed as

$$Y = \mathbf{C}\mathbf{X} + \mathbf{D}\mathbf{U} \tag{23}$$

where  $C$  is a coefficient matrix of vector  $X$  and  $D$  is a coefficient matrix of vector  $U$ .

### 3. Design of Vehicle Attitude Stability Controller

The ADRC method is used to design the vehicle attitude controller. ADRC consists of three main parts [29,30]: extended state observer (ESO), feedback controller, and disturbance rejection law.

The available system model information can be used to reduce the estimation time of the ESO and improve the ability of disturbance rejection. Accordingly, the jet action force is regarded as a model-assisted part, which is embedded in the ESO and integrated into the control law to achieve the desired output [31,32].

According to the derived vehicle dynamics equations, let  $x_1 = Z$ ,  $x_2 = \theta$ , and  $x_3 = \varphi$ . Thus, Equations (3)–(5) can be rewritten as follows:

$$\ddot{x}_1 = \ddot{Z} = f_1(Z \ \theta \ \varphi \ \dot{Z} \ \dot{\theta} \ \dot{\varphi} \ z_{r1}z_{r2} \cdots z_{r6}) - \frac{F_l \sin \alpha}{m_b} + \frac{U_1}{m_b} + \frac{U_2}{m_b} + \frac{U_3}{m_b} + \frac{U_4}{m_b} + \frac{U_5}{m_b} + \frac{U_6}{m_b} \tag{24}$$

$$\begin{aligned} \ddot{x}_2 = \ddot{\theta} = f_1(Z \ \theta \ \varphi \ \dot{Z} \ \dot{\theta} \ \dot{\varphi} \ z_{r1}z_{r2} \cdots z_{r6}) &+ \frac{F_l [\cos \alpha \sin \beta \sin \delta B + \sin \alpha (d - B \cos \delta)]}{I_\theta} \\ &- \frac{aU_1}{I_\theta} - \frac{aU_2}{I_\theta} + \frac{aU_3}{I_\theta} + \frac{aU_4}{I_\theta} + \frac{aU_5}{I_\theta} + \frac{aU_6}{I_\theta} \end{aligned} \tag{25}$$

$$\begin{aligned} \ddot{x}_3 = \ddot{\varphi} = f_1(Z \ \theta \ \varphi \ \dot{Z} \ \dot{\theta} \ \dot{\varphi} \ z_{r1}z_{r2} \cdots z_{r6}) &- \frac{F_l \cos \alpha \cos \beta \sin \delta B}{I_\varphi} \\ &+ \frac{lU_1}{2I_\varphi} - \frac{lU_2}{2I_\varphi} + \frac{lU_3}{2I_\varphi} - \frac{lU_4}{2I_\varphi} + \frac{lU_5}{2I_\varphi} - \frac{lU_6}{2I_\varphi} \end{aligned} \tag{26}$$

Let  $\mathbf{X} = [x_1 \ x_2 \ x_3]^T$ , take  $\mathbf{u} = [U_1 \ U_2 \ U_3 \ U_4 \ U_5 \ U_6]^T$  as the input of the suspension actuator, and take  $\mathbf{Y} = [x_1 \ x_2 \ x_3]^T$  as system output; the state space expression is

$$\begin{cases} \ddot{\mathbf{X}} = \mathbf{F}(Z \ \theta \ \varphi \ \dot{Z} \ \dot{\theta} \ \dot{\varphi} \ z_{r1}z_{r2} \cdots z_{r6}) + F_l \mathbf{H} + \mathbf{B}\mathbf{u} \\ \mathbf{Y} = \mathbf{X} \end{cases} \tag{27}$$

where

$$\mathbf{F}(Z \ \theta \ \varphi \ \dot{Z} \ \dot{\theta} \ \dot{\varphi} \ z_{r1}z_{r2} \cdots z_{r6}) = \begin{bmatrix} f_1(Z \ \theta \ \varphi \ \dot{Z} \ \dot{\theta} \ \dot{\varphi} \ z_{r1}z_{r2} \cdots z_{r6}) \\ f_2(Z \ \theta \ \varphi \ \dot{Z} \ \dot{\theta} \ \dot{\varphi} \ z_{r1}z_{r2} \cdots z_{r6}) \\ f_3(Z \ \theta \ \varphi \ \dot{Z} \ \dot{\theta} \ \dot{\varphi} \ z_{r1}z_{r2} \cdots z_{r6}) \end{bmatrix} \tag{28}$$

$$B = \begin{bmatrix} \frac{1}{m_b} & \frac{1}{m_b} & \frac{1}{m_b} & \frac{1}{m_b} & \frac{1}{m_b} & \frac{1}{m_b} \\ -\frac{a}{I_\theta} & -\frac{a}{I_\theta} & \frac{b}{I_\theta} & \frac{b}{I_\theta} & \frac{c}{I_\theta} & \frac{c}{I_\theta} \\ \frac{l}{2I_\varphi} & -\frac{l}{2I_\varphi} & \frac{l}{2I_\varphi} & -\frac{l}{2I_\varphi} & \frac{l}{2I_\varphi} & -\frac{l}{2I_\varphi} \end{bmatrix} \tag{29}$$

$$H = \begin{bmatrix} \frac{-\sin \alpha}{m_b} \\ \frac{\cos \alpha \sin \beta \sin \delta B + \sin \alpha (d - B \cos \delta)}{I_\theta} \\ \frac{-\cos \alpha \cos \beta \sin \delta B}{I_\varphi} \end{bmatrix} \tag{30}$$

The coupling between each suspension output force  $Bu$  in the above system is called “Static coupling”, and the coupling that exists in the Vehicle model is called the “Dynamic coupling”. Let  $S = Bu$  be the virtual output of the system; then, Equation (27) can be rewritten as

$$\begin{cases} \ddot{X} = F(Z \theta \varphi \dot{Z} \dot{\theta} \dot{\varphi} z_{r1} z_{r2} \cdots z_{r6}) + F_l H + S \\ Y = X \end{cases} \tag{31}$$

Therefore, the input–output relationship of the  $i$ th channel of the system is expressed as

$$\begin{cases} \ddot{x}_i = f_i(Z \theta \varphi \dot{Z} \dot{\theta} \dot{\varphi} z_{r1} z_{r2} \cdots z_{r6}) + F_l H_i + S_i \\ y_i = x_i \end{cases} \tag{32}$$

where  $i = (1,2,3)$ , respectively, represents the vertical displacement, the pitch angle, and the roll angle of the vehicle. In each channel, the relationship between the input and output is SISO, and the static coupling in the system is decoupled. Dynamic coupling and other disturbances are regarded as system disturbances, and a second-order extended state observer (ESO) is designed to estimate the system disturbance as follows:

$$\begin{cases} e_{i1} = Z_{i1} - y_{i1} \\ f_{ei1} = fal(e_{i1}, \zeta, h_i) \\ \dot{Z}_{i1} = Z_{i2} - \beta_{i1} e_{i1} \\ \dot{Z}_{i2} = Z_{i3} - \beta_{i2} f_{ei1} + F_l H_i + b_{i1} S_i \\ \dot{Z}_{i3} = -\beta_{i3} f_{ei1} \end{cases} \tag{33}$$

where  $e_{i1}$  is the output error of each channel;  $Z_{i3}$  is the estimated disturbance of the system;  $h_i$  is the length of the sampling step;  $Z_{i1}$  and  $Z_{i2}$  are system state observations;  $b_{i1}$  is the compensation factor;  $fal$  is the nonlinear feedback function;  $\beta_{i1}$ ,  $\beta_{i2}$ , and  $\beta_{i3}$  are adjustable parameters of the extended state observer. The parameters are adjusted by the Fibonacci series and engineering experience [33].

$$fal(e, \rho, h) = \begin{cases} |e|^\tau sign(e) & |e| \geq h \\ \frac{e}{h^{1-\tau}} & |e| < h \end{cases} \tag{34}$$

Design the state error control law as

$$\begin{cases} e_{i1} = v_{i1} - Z_{i1} \\ e_{i2} = v_{i2} - Z_{i2} \\ F_{0i} = \beta_1 fal(e_{i1}, \alpha_1, \rho) + \beta_2 fal(e_{i2}, \alpha_2, \rho) \\ F_i = F_{0i} - (Z_{i3} + F_l H_i) / b_{i1} \end{cases} \tag{35}$$

Where  $\beta_1$  and  $\beta_2$  are gains of the controller.

The principle of a single-channel MADRC is shown in Figure 2.

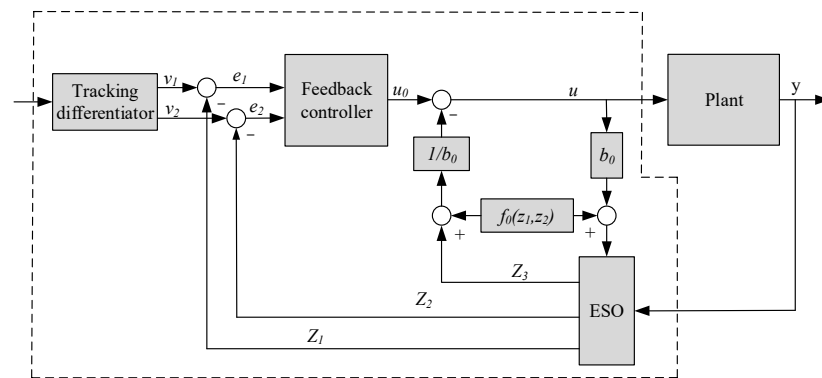


Figure 2. Principle of MADRC.

As the control objective of each channel is to stabilize vertical displacement, the pitch angle, and the roll angle, i.e.,  $v_{1i} = 0$ , a tracking differential does not need to be designed in the controller to extract the input.

Three virtual outputs  $S_i$  are calculated by the three ADRCs designed above, and the suspension system studied in this paper is a 6-input 3-output system. Therefore, the 3 outputs need to be decoupled. As the input coefficient matrix  $B$  of the system is irreversible, the output of the system is decoupled by solving the pseudo-inverse matrix of  $B$ . Let  $T = BT(BBT)^{-1}$ ; then, the input force of each actuator is  $U_j = TS_i$ , ( $i = 1,2,3; j = 1,2, \dots, 6$ ). The structure of the MADRC system of the vehicle is shown in Figure 3.

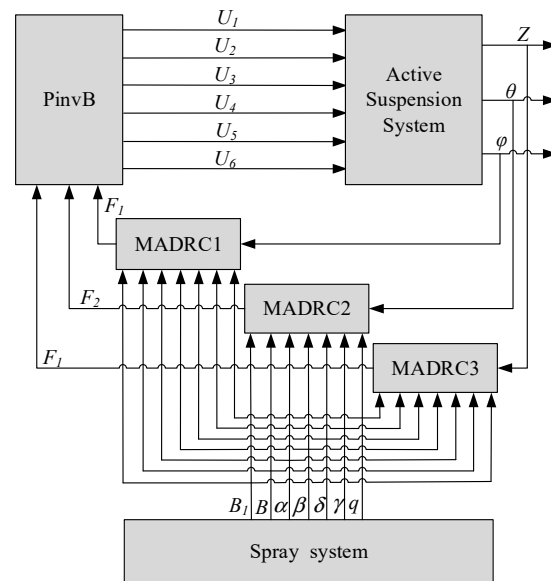


Figure 3. Structure of MADRC system.

Vertical, pitch, and roll controllers are designed using the MADRC integrated control strategy. The parameters of the spray system are added into the ESO, which reduces the estimation burden of the ESO, improves the system control performance, and realizes the adjustment and control of vehicle attitude.

#### 4. Simulation Analysis

To verify the effectiveness of the three designed controllers, the control effect of the active suspension system and passive suspension system is simulated. The required parameters in the vehicle simulation model are shown in Table 1.

**Table 1.** Main parameters of the vehicle.

Parameter	Symbol	Value	Unit
Sprung mass	$m_{a1}$	25,649	Kg
Boom mass	$m_{a2}$	4249	Kg
Unsprung mass	$m_w$	650	Kg
Stiffness of suspension spring	$k_s$	130,000	N/m
Damping of suspension	$c_s$	38,500	N/m
Stiffness coefficient of tire	$k_t$	$1.9 \times 10^6$	N/m
Equivalent pitching moment of inertia	$I_\varphi$	78,593	Kg m <sup>2</sup>
Equivalent rolling moment of inertia	$I_\phi$	26,506	Kg m <sup>2</sup>
Wheel tread	$l$	2.15	m
Distance of front axle and mass center of chassis	$a$	3.65	m
Distance of middle axle and mass center of chassis	$b$	1.05	m
Distance of rear axle and mass center of chassis	$c$	2.70	m
Distance of hinge of boom and mass center of chassis	$d$	3.12	m
Luffing angle of boom	$\delta$	85	°
Rotating angle of boom	$\gamma$	0	°
Length of boom	$B$	18	m
Distance of hinge point of boom and mass center of boom	$B_1$	8.4	m
Angle between jet reaction force and horizontal direction	$\alpha$	20	°
Angle between jet reaction force and vertical direction	$\beta$	45	°
Area of fire monitor outlet	$s$	$3.11 \times 10^{-3}$	m <sup>2</sup>

Random white noise as shown in Figure 4 is taken as the road excitation, the driving speed of the vehicle is set to 10 km/h, and the instantaneous flow rate of the fire monitor is set to a sinusoidal form with an amplitude of 0–120 L/min, as shown in Figure 5a. The simulation time is set to 10 s, and the simulation results of the output response of the vehicle attitude are shown in Figures 5b and 6.

Figures 5b and 6 show the comparison curves of vertical displacement, pitch angle, and roll angle of the mass center of the chassis. It can be seen from the figure that the vertical displacement, pitch angle, and roll angle of the integrated spray-active suspension system under MADRC control are significantly optimized compared with the conventional active suspension system under ADRC control and passive suspension.

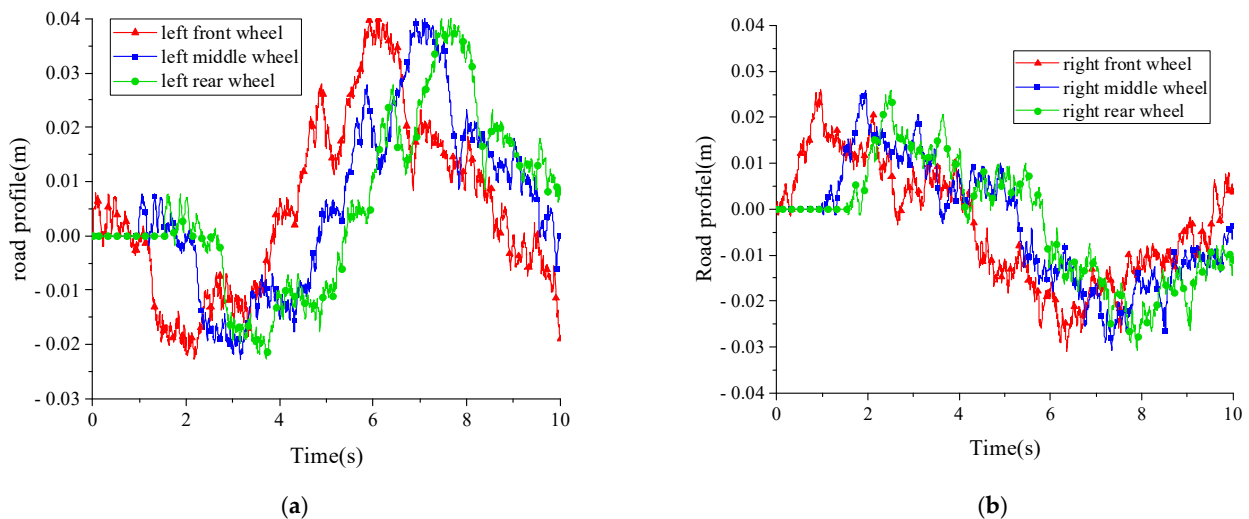


**Figure 4.** (a) Road profile of left side under stochastic signals; (b) road profile of right side under stochastic signals.

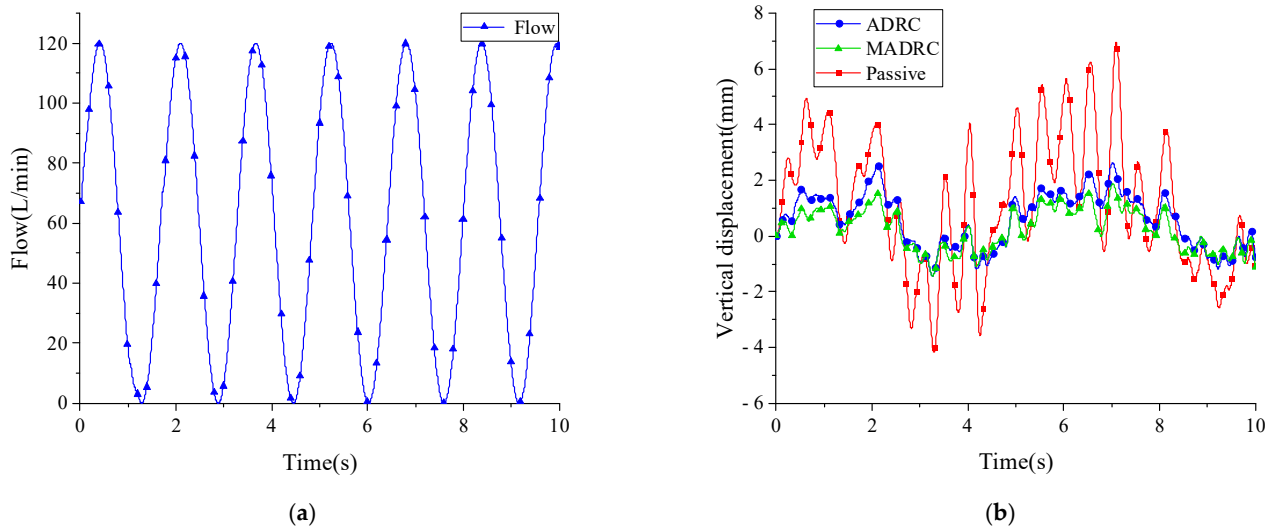


Figure 5. (a) Spray flow curve; (b) comparison curve of vehicle vertical displacement under stochastic signals.

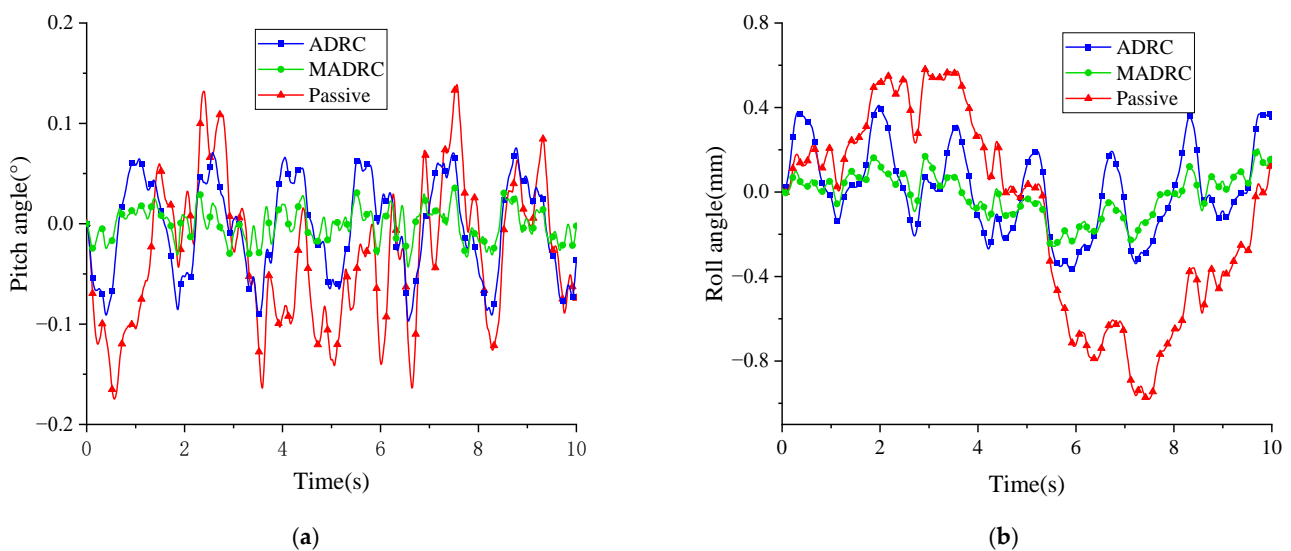


Figure 6. (a) Comparison curve of vehicle pitch angle under stochastic signals; (b) comparison curve of vehicle roll angle under stochastic signals.

The quantitative analysis of the curves is carried out, and the root-mean-square values of the vertical displacement, pitch angle, and roll angle of the vehicle are calculated. The results are shown in Table 2.

Table 2. Root-mean-square value of vehicle attitude under stochastic signals.

	Passive	ADRC	MADRC
vertical displacement (mm)	2.638	1.140(↓56.78%)	0.786(↓70.20%)
pitch angle	0.077	0.048(↓37.84%)	0.016(↓79.22%)
roll angle	0.477	0.205(↓56.92%)	0.107(↓77.57%)

It can be seen from Table 2 that compared with the passive suspension system, the vertical displacement, pitch angle, and roll angle of the traditional active suspension system under ADRC control decrease by 56.78%, 37.84%, and 56.92%, respectively, and those of the integrated spray-active suspension system under MADRC control are further reduced

by 13.42%, 41.38%, and 20.65%, respectively, compared with the passive suspension system. Each evaluation index is reduced by 70.20%, 79.22%, and 77.57% respectively.

In order to verify the advantages of the integrated model compared with the traditional suspension model in the literature [21], sinusoidal wave road excitation is implemented in the simulation. The road excitation of the two sides of the vehicle is shown in Figure 7. Other required parameters in the simulation model are the same as before. Figures 8 and 9 show the comparison curves of vertical displacement, pitch angle, and roll angle of the mass center of the chassis, and the peak–peak values are presented in Table 3.

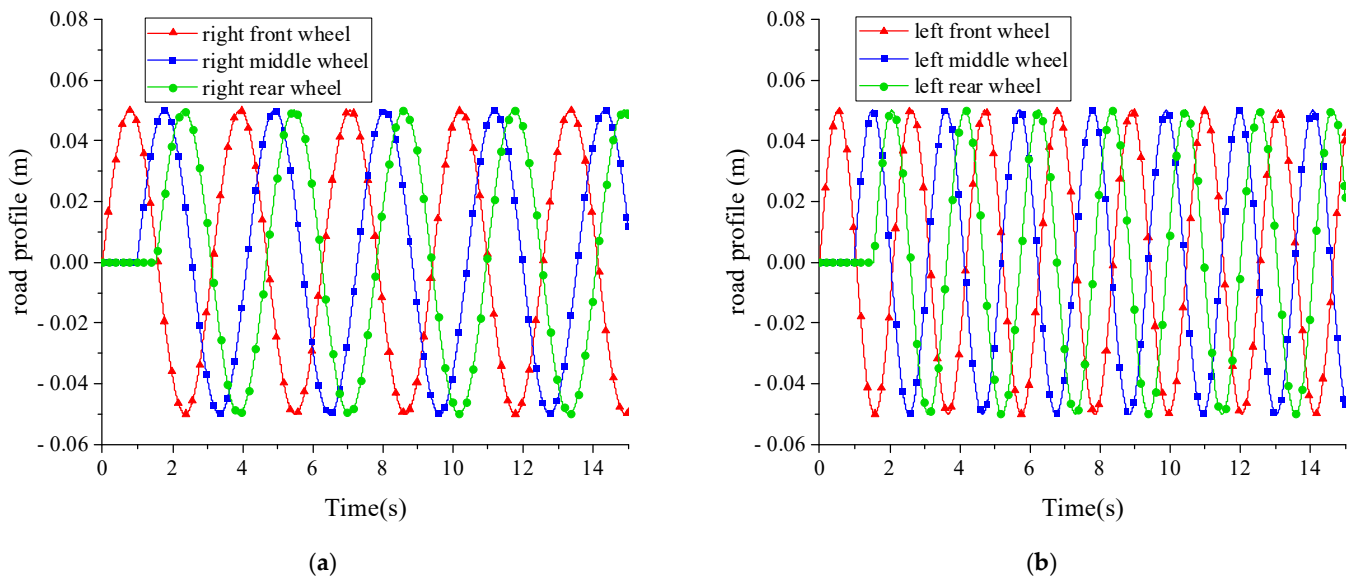


Figure 7. (a) Road profile of left side under sinusoidal signals; (b) road profile of right side under sinusoidal signals.

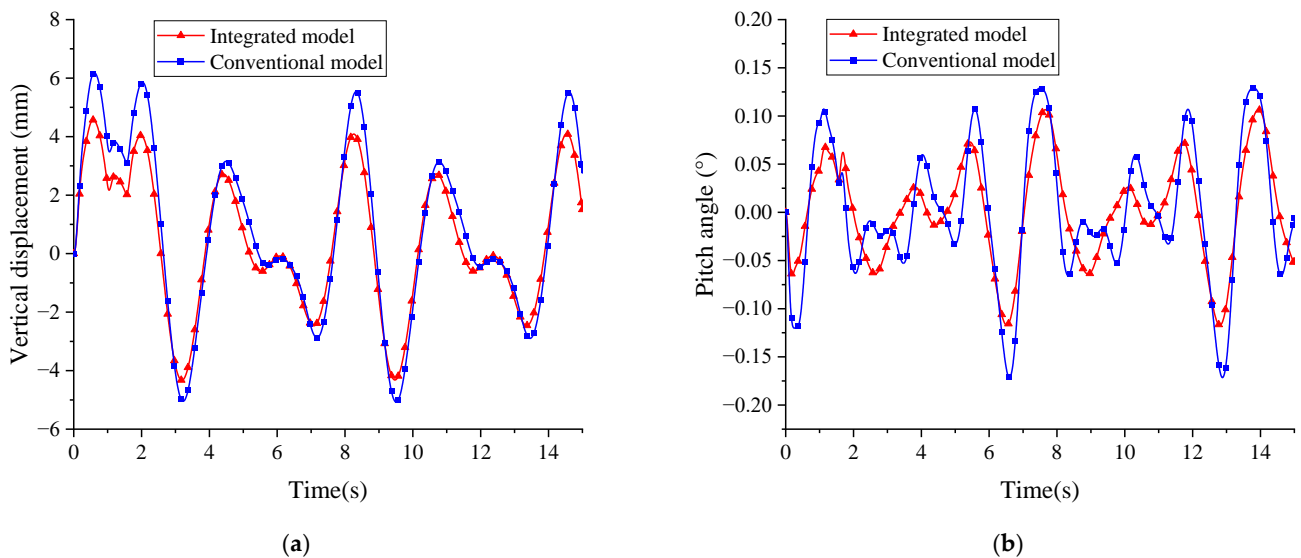


Figure 8. (a) Comparison curve of vehicle vertical displacement under sinusoidal signals; (b) comparison curve of vehicle pitch angle under sinusoidal signals.

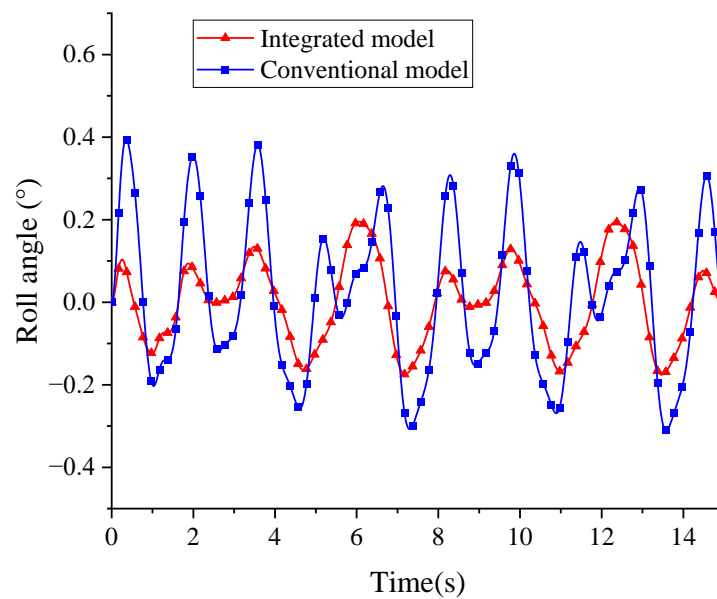


Figure 9. Comparison curve of vehicle roll angle under sinusoidal signals.

Table 3. Peak–peak value of vehicle attitude under sinusoidal signals.

	Vertical Displacement/mm	Pitch Angle/°	Roll Angle/°
Conventional model	11.17	0.29	0.68
Integrated model	8.96	0.23	0.37
Difference	2.21	0.06	0.31
Performance improvement	19.8%	20.7%	45.6%

As shown in the previous figures, the proposed spray-active suspensions integrated model presents a better performance when compared with the conventional active suspension model. The vertical displacement, pitch angle, and roll angle of the vehicle are decreased by 19.8%, 20.7%, and 45.6%, respectively.

### 5. Experiments and Results Analysis

In order to further verify the effectiveness of the controller for improving the vehicle attitude, a barrier-crossing experiment was carried out on a water tower fire truck JP32G. The suspension system of the vehicle has active and passive working modes. The active mode is driven by a hydraulic servo and the passive mode is the hydro-pneumatic suspension system. The structure of the integrated control system is shown in Figure 10.

The controller uses a SCM9022 main board, which meets the standard PC/104 bus standard. The data acquisition system uses a ADT882-AT expansion board and provides 32 16-bit analog channels at a sampling speed of 200 kHz. The inertia measuring unit adopts an MTi 300AHRS IMU and the pressure sensor uses a PM95B series pressure transmitter with a measuring range of 0–40 MPa and accuracy of <0.25%. The actuator is a hydraulic cylinder;  $p_{1i}$  and  $p_{2i}$  ( $i = 1, 2, \dots, 6$ ) are pressures of the rod and rodless cavity, respectively. Basic parameters of the tested vehicle are shown in Table 4.

The water spray obstacle crossing test was carried out on the water tower fire truck working in the integrated spray-active suspension system mode and the passive suspension mode. The test pavement was cement pavement and tire excitation was achieved by setting triangular obstacles on the pavement. Figure 11 shows the water spray obstacle crossing test vehicle and site. The triangular obstacle is shown in Figure 12.

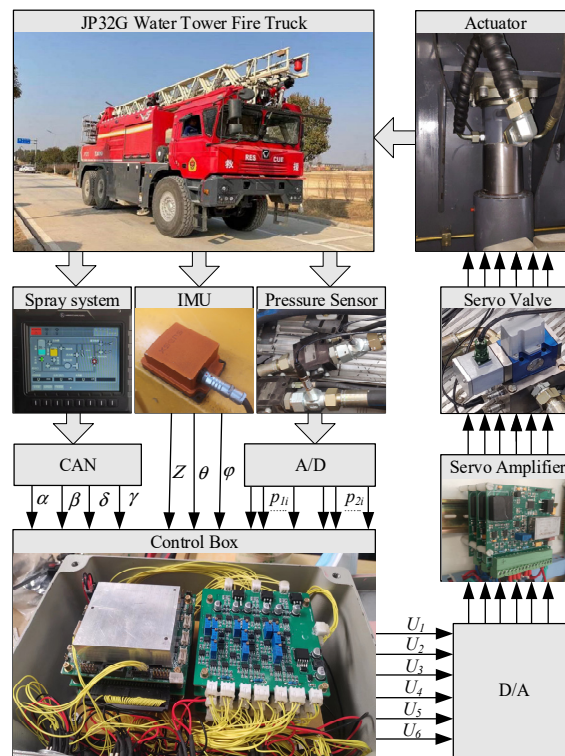


Figure 10. Structure of the integrated control system.

Table 4. Main parameters of the tested vehicle.

Parameters	Value
Vehicle type	JP32G
Weight/kg	29,898
Chassis type	XPD36
Number of axles	3
Number of wheels	6
Number of drive wheels	6
Tire specification	445/95R25
Wheelbase of first and second axle /mm	4700
Wheelbase of second and third axle /mm	1650
Wheel tread /mm	2150



Figure 11. Test vehicle and site.

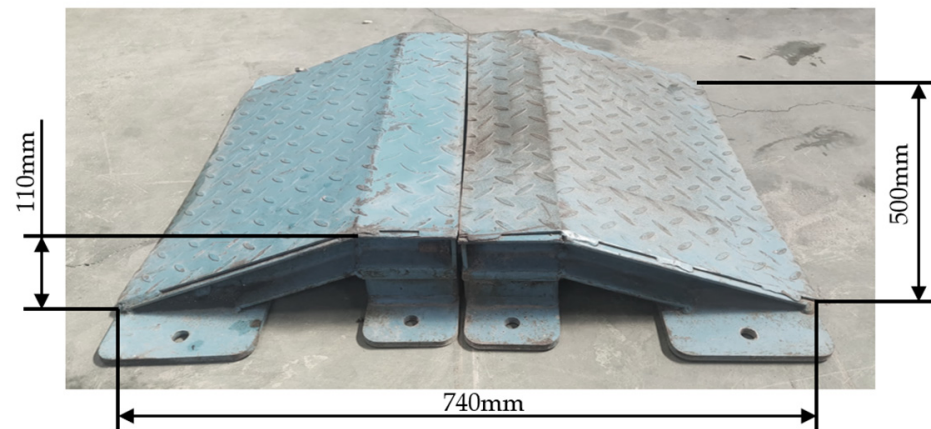


Figure 12. Triangle obstacle.

During the experiment, triangular obstacles were placed on one or two sides in front of the vehicle. The control program was started, the vehicle was moved over the triangular obstacles, and changes in body pitch and roll angle were recorded. The control procedure was switched off, the suspension system was switched to hydro-pneumatic passive suspension, the vehicle was moved over the triangular obstacles at the same speed and manner, and the pitch and roll angle of the vehicle were recorded.

Figure 13 shows the pitch and roll angle curves of the vehicle with the wheels on one side crossing a triangular obstacle at a speed of 3.2 km/h. Figure 14 shows the pitch and roll angle curves of the vehicle with the wheels of two sides crossing a triangular obstacle at a speed of 3.2 km/h.

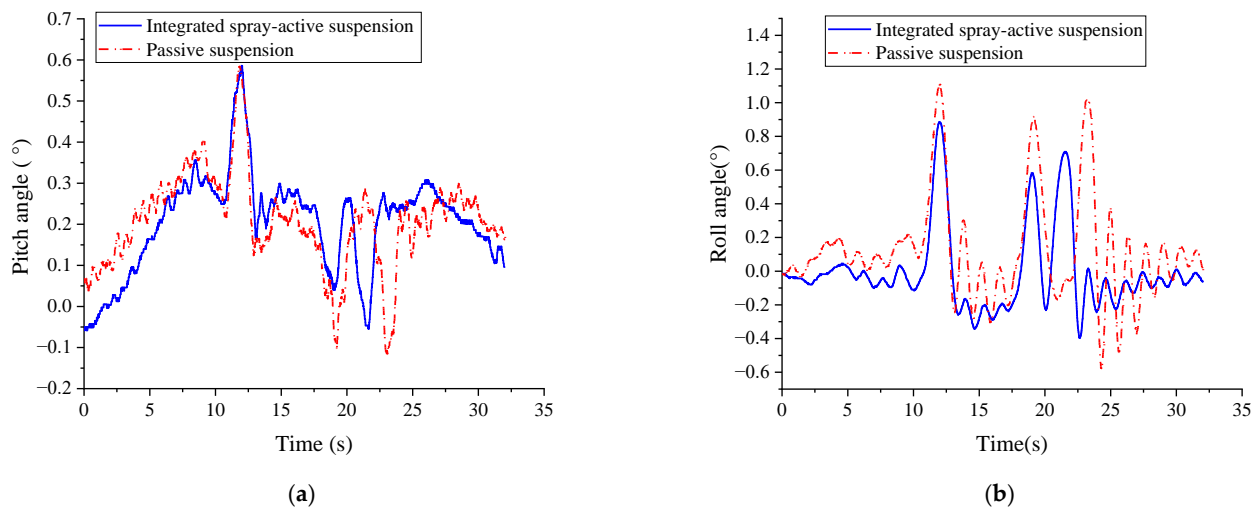
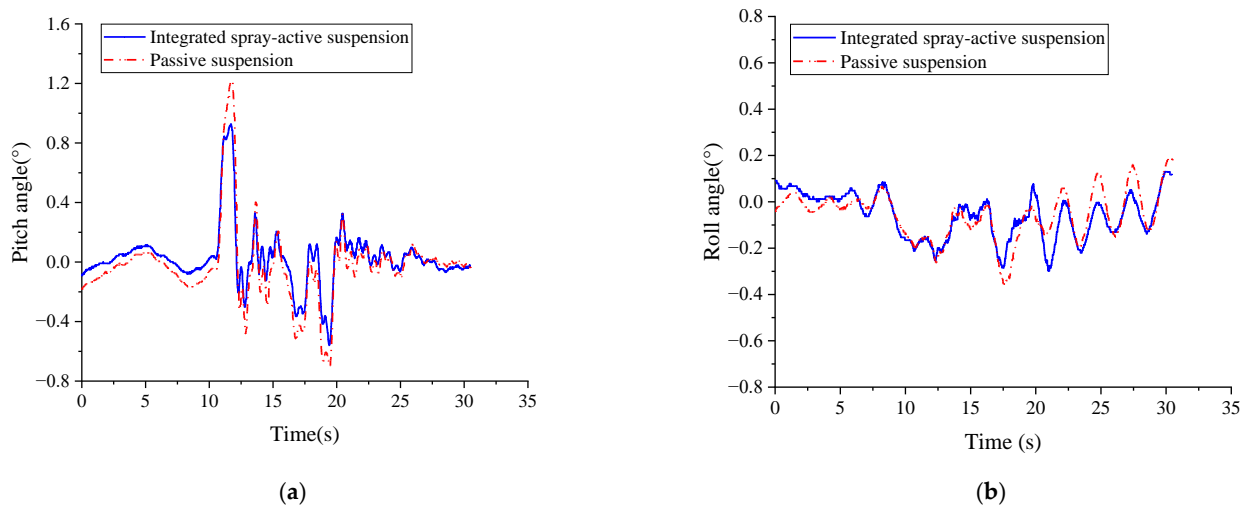


Figure 13. (a) Pitch angle comparison curve of wheel-crossing obstacle on one side; (b) roll angle comparison curve of wheel-crossing obstacle on one side.

From the test comparison curves, it can be seen that the integrated spray-active suspension under MADRC control significantly improves the pitch and roll stability of the vehicle compared with the passive suspension system when the vehicle passes through uneven road surfaces.

Quantitative analysis of Figures 13 and 14 is carried out, and the peak–peak value of vehicle attitude is shown in Table 5.



**Figure 14.** (a) Pitch angle comparison curve of wheel-crossing obstacle on two sides; (b) roll angle comparison curve of wheel-crossing obstacle on two sides.

**Table 5.** Peak–peak value of vehicle attitude.

	Pitch Angle/°		Roll Angle/°	
	One side	Two sides	One side	Two sides
Passive suspension	0.73	1.85	1.68	0.55
Integrated spray-active suspension	0.65	1.41	1.29	0.46
Difference	0.08	0.44	0.39	0.08
Performance improvement	10.9%	23.7%	23.2%	16.3%

It can be seen from Table 5 that compared with the passive suspension system, the peak–peak values of pitch angle and roll angle of the integrated spray-active suspension system under MADRC control decrease by 10.9% and 23.2%, respectively, when the vehicle runs over triangular obstacles on one side, and decrease by 23.7% and 16.3%, respectively, when the vehicle runs over triangular obstacles on two sides.

### 6. Discussion

In the 13-DOF integrated dynamic model studied in this paper, it is assumed that the boom is a rigid body, but in fact, the boom will produce large deformation under the torque due to the clearance and compliance of the boom. This directly affects the spray angle of the fire monitor at the top of the boom and the action point of the spray reaction force, so the elastic deformation of the boom is a critical factor to be considered in future work.

A model-assisted nonlinear disturbance rejection controller is proposed and applied to water tower fire trucks. The innovation lies in introducing the known vehicle dynamic information into the extended state observer to reduce the bandwidth burden of the observer and improve the overall control performance. Due to the complicated theoretical analysis of the nonlinear ADRC (the nonlinearity of the *fal* function), the stability analysis of the disturbance rejection controller is still in the development stage, and there is relatively little related theoretical research. Analysis methods include the self-stable region approach [34,35], frequency domain method [36,37], and Popov hyperstability theory [38,39]. The difficulty of stability analysis theory leads to the limited application of nonlinear ADRC. However, it has been proved in practice that the nonlinear ADRC can stabilize the system and has higher convergence efficiency than the linear form. From the perspective of engineering application, this paper preliminarily explores its application in the field of active suspension. However, the stability analysis of the model-assisted expanding state observer is still under further study, and this is also work to be carried out in the future.

## 7. Conclusions

In this paper, a 13-DOF integrated spray-active suspension dynamic model of the water tower fire truck is established. The MADRC control method is used to design the vehicle attitude controller, and computer simulation and real vehicle tests are carried out.

The simulation results show that when the vehicle speed is 10 km/h, the vertical displacement, pitching angle, and roll angle of the integrated spray-active suspension system under the MADRC control decrease by 70.20%, 79.22%, and 77.57%, respectively, compared with the passive suspension system, and decrease by 19.8%, 20.7%, and 45.6%, respectively, compared with the conventional active suspension model under sinusoidal wave road excitation.

The experimental results show that when the vehicle runs over the triangular obstacle on one side and two sides in the integrated spray-active suspension mode, the peak–peak values of pitch angle and roll angle are reduced by 10.9% and 23.2%, and 23.7% and 16.3%, respectively, compared with the passive hydro pneumatic suspension.

**Author Contributions:** Conceptualization, D.Z. and J.Z.; methodology, D.Z. and J.Z.; software, S.L.; validation, S.L. and Z.Z.; investigation, D.Z. and J.Z.; resources, D.Z. and S.L.; formal analysis, J.C.; data curation, Z.Z.; writing—original draft preparation, G.L. and J.C.; writing—review and editing, D.Z. and J.Z.; funding acquisition, D.Z. All authors have read and agreed to the published version of the manuscript.

**Funding:** This research was funded by Regional Innovation and Development Funds of the National Natural Science Foundation of China (U20A20332), and Innovative research group of the Natural Science Foundation of Hebei Province, China (E202003174).

**Institutional Review Board Statement:** Not applicable.

**Informed Consent Statement:** Not applicable.

**Data Availability Statement:** Not applicable.

**Conflicts of Interest:** The authors declare no conflict of interest.

## References

1. He, M.; Jia, C. Analysis on roll stability of urban main battle fire truck under working conditions. *Fire Sci. Technol.* **2018**, *37*, 3.
2. Zirkohi, M.M.; Lin, T. Interval type-2 fuzzy-neural network indirect adaptive sliding mode control for an active suspension system. *Nonlinear Dyn.* **2015**, *79*, 513–526. [[CrossRef](#)]
3. Gohrle, C.; Schindler, A.; Wagner, A.; Sawodny, O. Road Profile Estimation and Preview Control for Low-Bandwidth Active Suspension Systems. *IEEE/ASME Trans. Mechatron.* **2015**, *20*, 2299–2310. [[CrossRef](#)]
4. Pan, H.; Jing, X.; Sun, W. Robust finite-time tracking control for nonlinear suspension systems via disturbance compensation. *Mech. Syst. Signal Process.* **2017**, *88*, 49–61. [[CrossRef](#)]
5. Du, M.; Zhao, D.; Yang, B.; Wang, L. Terminal sliding mode control for full vehicle active suspension systems. *J. Mech. Sci. Technol.* **2018**, *32*, 2851–2866. [[CrossRef](#)]
6. Mustafa, G.I.Y.; Wang, H.P.; Tian, Y. Vibration control of an active vehicle suspension systems using optimized model-free fuzzy logic controller based on time delay estimation. *Adv. Eng. Softw.* **2019**, *127*, 141–149. [[CrossRef](#)]
7. Zhang, Y.; Liu, Y.; Liu, L. Minimal learning parameters-based adaptive neural control for vehicle active suspensions with input saturation. *Neurocomputing* **2020**, *396*, 153–161. [[CrossRef](#)]
8. Yao, J.; Wang, M.; Li, Z.; Jia, Y. Research on Model Predictive Control for Automobile Active Tilt Based on Active Suspension. *Energies* **2021**, *14*, 671. [[CrossRef](#)]
9. Li, P.; Lam, J.; Cheung, K.C. Multi-objective control for active vehicle suspension with wheelbase preview. *J. Sound Vib.* **2014**, *333*, 5269–5282. [[CrossRef](#)]
10. Liu, Y.; Zeng, Q.; Tong, S.; Chen, C.L.P.; Liu, L. Adaptive Neural Network Control for Active Suspension Systems with Time-Varying Vertical Displacement and Speed Constraints. *IEEE Trans. Ind. Electron.* **2019**, *66*, 9458–9466. [[CrossRef](#)]
11. Liu, Y.; Zeng, Q.; Tong, S.; Chen, C.L.P.; Liu, L. Actuator Failure Compensation-Based Adaptive Control of Active Suspension Systems with Prescribed Performance. *IEEE Trans. Ind. Electron.* **2020**, *67*, 7044–7053. [[CrossRef](#)]
12. Li, H.; Liu, H.; Gao, H.; Shi, P. Reliable Fuzzy Control for Active Suspension Systems with Actuator Delay and Fault. *IEEE Trans. Fuzzy Syst.* **2012**, *20*, 342–357. [[CrossRef](#)]
13. Li, H.; Zhang, Z.; Yan, H.; Xie, X. Adaptive Event-Triggered Fuzzy Control for Uncertain Active Suspension Systems. *IEEE Trans. Cybern.* **2019**, *49*, 4388–4397. [[CrossRef](#)] [[PubMed](#)]

14. Kim, H.; Lee, H. Height and Leveling Control of Automotive Air Suspension System Using Sliding Mode Approach. *IEEE Trans. Veh. Technol.* **2011**, *60*, 2027–2041.
15. Youn, I.; Im, J.; Tomizuka, M. Level and attitude control of the active suspension system with integral and derivative action. *Veh. Syst. Dyn.* **2006**, *44*, 659–674. [[CrossRef](#)]
16. Van der Westhuizen, S.F.; Els, P.S. Slow active suspension control for rollover prevention. *J. Terramech.* **2013**, *50*, 29–36. [[CrossRef](#)]
17. Tchamna, R.; Lee, M.; Youn, I. Attitude control of full vehicle using variable stiffness suspension control. *Optim. Control Appl. Methods* **2015**, *36*, 936–952. [[CrossRef](#)]
18. Chen, H.; Gong, M.; Zhao, D.; Zhu, J. Body attitude control strategy based on road level for heavy rescue vehicles. *Proc. Inst. Mech. Eng. Part D* **2021**, *235*, 1351–1363. [[CrossRef](#)]
19. Youn, I.; Wu, L.; Youn, E.; Tomizuka, M. Attitude motion control of the active suspension system with tracking controller. *Int. J. Automot. Technol.* **2015**, *16*, 593–601. [[CrossRef](#)]
20. Sun, J.; Li, W.; He, M. Analysis of Fire Water Monitor Jet Reaction Forces and Their Influences on the Roll Stabilities of Urban Firefighting Vehicle. *Fire Technol.* **2019**, *55*, 2547–2566. [[CrossRef](#)]
21. Gong, M.; Chen, H. Variable damping control strategy of a semi-active suspension based on the actuator motion state. *J. Low Freq. Noise Vib. Act. Control* **2020**, *39*, 787–802. [[CrossRef](#)]
22. Wang, R.; Sheng, F.; Ding, R.; Meng, X.; Sun, Z. Vehicle attitude compensation control of magneto-rheological semi-active suspension based on state observer. *Proc. Inst. Mech. Eng. Part D* **2021**, *235*, 3299–3313. [[CrossRef](#)]
23. Li, B.; Zheng, G.; Wang, Z. Attitude Control of the Vehicle with Six In-Wheel Drive and Adaptive Hydro Pneumatic Suspensions. In Proceedings of the WCX SAE World Congress Experience, Detroit, MI, USA, 9–11 April 2019.
24. Guo, Q.; Zhao, D.; Zhao, X.; Li, Z.; Shi, X. Active Suspension Control Strategy of Multi-Axle Emergency Rescue Vehicle Based on Inertial Measurement Unit. *Sensors* **2021**, *21*, 6877. [[CrossRef](#)] [[PubMed](#)]
25. Zeng, Q.; Ma, D.; Zhao, J. Adaptive Aperiodic Intermittent Control for Nonlinear Active Suspension Systems. In Proceedings of the Chinese Control Conference, Shanghai, China, 26–28 July 2021; pp. 1437–1441.
26. Khodamipour, G.; Khorashadizadeh, S.; Farshad, M. Observer-based adaptive control of robot manipulators using reinforcement learning and the Fourier series expansion. *Trans. Inst. Meas. Control* **2021**, *43*, 2307–2320. [[CrossRef](#)]
27. Izadbakhsh, A.; Khorashadizadeh, S.; Kheirkhahan, P. Tracking Control of Electrically Driven Robots Using a Model-free Observer. *Robotica* **2018**, *37*, 729–755. [[CrossRef](#)]
28. Liu, B. Calculation of Blowdown Thrust Force due to The Rupture of Main Pipe in Nuclear Power Plant. Ph.D. Thesis, Harbin Institute of Technology, Harbin, China, 2014.
29. Hasbullah, F.; Faris, W.F. Simulation of disturbance rejection control of half-car active suspension system using active disturbance rejection control with decoupling transformation. *J. Phys. Conf. Ser.* **2017**, *949*, 12025. [[CrossRef](#)]
30. Herbst, G. A Simulative Study on Active Disturbance Rejection Control (ADRC) as a Control Tool for Practitioners. *Electronics* **2013**, *2*, 246–279. [[CrossRef](#)]
31. Li, S.; Cao, M.; Li, J.; Cao, J.; Lin, Z. Sensorless-Based Active Disturbance Rejection Control for a Wind Energy Conversion System with Permanent Magnet Synchronous Generator. *IEEE Access* **2019**, *7*, 122663–122674. [[CrossRef](#)]
32. Sobhy, A.; Lei, D. Model-assisted active disturbance rejection controller for maximum efficiency schemes of DFIG-based wind turbines. *Int. Trans. Electr. Energy Syst.* **2021**, *31*, e13107. [[CrossRef](#)]
33. Wang, L.; Zhao, D.; Liu, F.; Liu, Q.; Meng, F. Linear active disturbance rejection control for electro-hydraulic proportional position synchronous. *Control Theory Appl.* **2018**, *35*, 1618–1625.
34. Huang, Y. A new synthesis method for uncertain systems the Self-Stable Region approach. *Int. J. Syst. Sci.* **1999**, *30*, 33–38. [[CrossRef](#)]
35. Zhao, L.; Yang, Y.; Xia, Y.; Liu, Z. Active Disturbance Rejection Position Control for a Magnetic Rodless Pneumatic Cylinder. *IRE Trans. Ind. Electron.* **2015**, *62*, 5838–5846. [[CrossRef](#)]
36. Li, J.; Qi, X.; Xia, Y.; Pu, F.; Chang, K. Frequency domain stability analysis of nonlinear active disturbance rejection control system. *ISA Trans.* **2015**, *56*, 188–195. [[CrossRef](#)] [[PubMed](#)]
37. Wu, D.; Chen, K. Limit cycle analysis of active disturbance rejection control system with two nonlinearities. *ISA Trans.* **2014**, *53*, 947–954. [[CrossRef](#)] [[PubMed](#)]
38. Li, J.; Xia, Y.; Qi, X.; Gao, Z. On the necessity, Scheme, and Basis of the Linear-Nonlinear Switching in Active Disturbance Rejection Control. *IRE Trans. Ind. Electron.* **2017**, *64*, 1425–1435. [[CrossRef](#)]
39. Li, J.; Xia, Y.; Qi, X.; Zhao, P. Robust absolute stability analysis for interval nonlinear active disturbance rejection based control system. *ISA Trans.* **2017**, *69*, 122–130. [[CrossRef](#)] [[PubMed](#)]